Magnetosphere - Ionosphere Coupling: Sub-auroral Heating of the Topside Ionospheric Electrons

C. Gurgiolo,[1] B. R. Sandel,[2] J. D. Perez,[3] D. G. Mitchell,[4] C. J. Pollock,[5]

and B. A. Larsen[6]

C. Gurgiolo, Bitterroot Basic Research Inc., 837 Westside Road, Hamilton, MT 59840, USA (chris@gurgiolo.com)

B. R. Sandel, Lunar and Planetary Laboratory, The University of Arizona, Sonett Space Sciences Building, 1541 East University Boulevard, Tuscon, AZ 85721-0063, USA (sandel@arizona.edu)

J. D. Perez, Physics Department, Auburn University, Auburn, AL 36849, USA (perez@physics.auburn.edu)

D. G. Mitchell, Applied Physics Laboratory, Johns Hopkins University, Johns Hopkins Road, Laurel, MD 20723, USA (Donald.G.Mitchell@jhuapl.edu)

C. J. Pollock, Southwest Research Institute, P. O. Drawer 28510, San Antonio, TX 78228-0510, USA (CPollock@swri.edu)

B. A. Larsen, Department of Physics, Space Science and Engineering Laboratory, P. O. Box 173840, Montana State University, Bozeman, MT 59717-3840, USA (larsen@ssel.montana.edu)

[1]Bitterroot Basic Research, Hamilton, MT

Abstract. The overlap of the ring-current with the outer plasmasphere is thought to play a major roll in the observations of storm-time related increases in the sub-auroral ambient topside electron temperatures. Instabilities generated within the overlap region, Coulomb collisions of plasmaspheric electrons with the ring-current ions, and charge exchange are all thought to work either individually or together to generate a downward directed heat flux which produces the increase in temperature. Which of these processes, if any, plays the more dominant role in the magnetospheric-ionospheric coupling has been the topic of many papers. The purpose of this paper is to present the first set of global, simultaneous observations of the ring-current and plas-

[2]Lunar and Planetary Laboratory, The University of Arizona, Tuscon, AZ

[3]Physics Department, Auburn University, Auburn, AL

[4]Applied Physics Laboratory, John Hopkins University, Laurel, MD

[5]Southwest Research Institute, San Antonio, TX

[6]Department of Physics, Montana State University, Bozeman, MT

masphere during storm time conditions together with in-situ measurements of the local topside ionospheric ambient electron temperature.

1. Introduction

Anomalous heating of the topside ambient sub-auroral electrons during storm-time conditions is thought to be a consequence of a downward heat flux generated within the overlap of ring current and plasmasphere. The heating more than likely originates in the decay of the ring current [*Fok et al.*, 1991] and is best known as the source of the Stable Auroral Red (SAR) arc [*Norton and Findley*, 1969; *Chandra et al.*, 1972]. Indeed much of the work focusing on the anomalous heating and its source is found in papers investigating either ring current decay or SAR arcs. In a way using the connection between SAR arcs and the thermal enhancements is deceiving. The fact that SAR arcs are not able to be observed on the dayside over the dayglow means that much of the theory and analysis has been based on conditions applicable to the pre and post midnight sectors. In addition the close association of SAR arcs with the plasmapause has focused the study of heating mechanisms on those which would be active in this region.*Kozyra et al.* [1982] have shown that the heatflux heating is a necessary but not a sufficient condition to produce a SAR arc. Conjugate satellite and ground observations show that SAR arcs rarely exists over the entire region of the thermal enhancement but are generally localized within an electron trough [*Foster et al.*, 1994] where the heating is increased due to the lower local density and more likely to reach the treshold necessary for excitation of the emission.

Multiple mechanisms have been proposed to create the heat flux responsible for the anomalous increases in the ionospheric electron temperature. All are based on a ring current interaction with the plasmasphere and generally benchmarked against their potential to raise the ionospheric electron temperature above the threshold necesary to produce a

SAR arc. *Cole* [1965, 1975] used Coulomb collisions of the plasmaspheric electrons with the ring current H^+ ions to produce a heated plasmaspheric electron population with collisional heat conductance used to establish the downward heat flux.*Kozyra et al.* [1987] extended this to include Coulomb collisions between the plasmaspheric electrons and energetic ring current O^+ ions but left the method of heat transfer open. Measurements of magnetospheric conditions during several observed SAR arcs showed that coulomb collisions could produce the necessary heating to drive the emissions. *Fok et al.* [1993] in a two-dimensional simulation study of ring current decay presented a global picture of the heating produced by Coulomb collisions concluding that even in dawn sector sufficient heat flux would be generated for SAR arc production.

Cornwall et al. [1971] suggested heating the plasmaspheric electrons through resonant Landau damping of H^+generated ion cyclotron waves. *Thorne and Horne* [1997] extended this to include O^+generated ion cyclotron waves. Direct scattering of the electrons into the loss cone coupled with conduction by collisionless strong diffusion provides the mechanism to transport the heat into the upper ionosphere. Under nominal conditions heating by ion cyclotron waves was shown to be able to supply sufficient heat to drive a generic SAR arc. Evidence of ion cyclotron waves in association with ionospheric heating events have been reported by *Lundblad and Søraas* [1978] and *Erlandson et al.* [1993]. Both *Jordanova et al.* [2001] and *Khazanov et al.* [2003] have included the growth rate of ion cyclotron waves in two-dimensional ring current models. Simulations using actual storm time inputs show a strong growth in the ion cyclotron waves in the post noon and pre midnight sectors at the start of the main phase with gradual extension into the noon and midnight sectors as the storm progresses.

Hasagawa and Mima [1978] proposed the possibility of in-situ heating by kinetic Alfvén waves. Unlike either Coulomb collisions or ion cyclotron waves, the heating is accomplished by direct acceleration of the plasmaspheric electrons into the ionosphere by the parallel electric field associated with the wave. *Lanzerotti et al.* [1978] have reported the presence of kinetic Alfvén waves in conjunction with SAR arcs.

There is no reason to opt for one mechanism over another. Undoubtedly under the proper conditions each will play a part in the coupling of the ring current to the ionosphere either alone or in concert with the others. The goal is to understand when a mechanism might be expected to be active and what its role in the coupling is.

This points to one of the outstanding deficiencies in the study of the coupling of the ring current to the ionosphere; the lack of concurrent and conjugate magnetospheric and ionospheric plasma measurements over complete anomalous heating events. With few exceptions most investigations are based on one set of measurements with nominal values and positions for the remaining sets. As we show here, the assumption made by many that the observed ionospheric heating occurs at the plasmapause is not necessarily true.

This paper presents a global view of the plasmasphere - ring current system during the 2001 June 18/19 (Days 169-170) storm. This was a small storm having a well defined onset and long recovery phase. We combine data from the IMAGE and DMSP satellites to have concurrent and conjugate plasma measurements from the plasmasphere, ring current and topside ionosphere. IMAGE is used to provide 2-D mappings of the plasma conditions in the geomagnetic equatorial plane out to 8 R_E for the ring-current ions and out to 6 R_E for the plasmaspheric He^+ ions while DMSP provides in-situ measurements of the ionospheric conditions at 800 km in both the dusk and dawn sectors. Data from the three DMSP

satellites (F12, F13, F15) provide over 100 crossings of the plasmasphere during the times when the IMAGE spacecraft is at an altitude giving full coverage of the geomagnetic equatorial plane. Plots of the equatorial ion flux and plasmaspheric He^+ density along the DMSP orbit tracks allow direct comparison of the states of the three overlapping plasma populations along the satellite track. This is the first time conditions across entire sub-auroral heating events have been studied with supporting conjugate magnetospheric observations.

2. Data

We use data from multiple experiments onboard the IMAGE and DMSP F-12, F-13, and F-15, satellites. Data from the IMAGE spacecraft provide 2-D coverage of the ring current and plasmasphere in the geomagnetic equatorial plane while DMSP provides in-situ monitoring of the ionospheric conditions including the ambient electron density and temperature and the energetic precipitating electrons and ions.

IMAGE was launched in March 2000 into an elliptical orbit of 0.15 x 7.2 RE with a 14.2-hour orbital period. The spacecraft has a 2-minute spin period that sets the temporal resolution of most measurements. The highly elliptical orbit provides long stretches of time with favorable observing geometry, that is, with lines of sight nearly perpendicular to the to the plane of the geomagnetic equator. This study makes extensive use of three IMAGE data sets.

The Extreme Ultraviolet Imager (EUV) [*Sandel et al.*, 2000] measures the brightness of the He^+ 30.4-nm emission from the plasmasphere with a spatial resolution of 0.6 degree (about 0.1 R_E) and a time resolution of 5 spins of the satellite (about 10 minutes). The measured brightness is directly proportional to the column abundance of He^+ along the

lines of sight corresponding to each pixel. For this work, we invert the images of He^+ column abundance to maps of He^+ density in the plane of the geomagnetic equator. We describe the inversion method that we have developed especially for this purpose in the next section.

Both the High and Medium Energy Neutral Atom imagers (HENA and MENA) return images of neutral atom fluxes. HENA [*Mitchell et al.*, 2000] operates in the $10 - 500$ keV/nucleon range while MENA [*Pollock et al.*, 2000] operates in the 1 to 70 keV/nucleon range. Both experiments resolve both energy and mass. Inversions of the neutral atom images (NAI) provide global 2-D distributions of the ion flux in the geomagnetic equatorial plane. The basic inversion methods are covered in *Roelof and Skinner* [2000] and *Perez et al.* [2000] and are not discussed in the paper. To synchronize the NAI and the EUV inverted data, the NAIs are integrated for 5 spins prior to inversion. This has an added bonus of increasing the statistics in the NAIs.

The DMSP satellites all follow circular polar orbits with a nominal altitude of 830 km and an orbital period of 101 minutes. Orbits are oriented either day/night (F-12, F-15) or dawn/dusk (F-13). The satellites carry identical complements of instruments.

The DMSP Special Sensor for Ions and Electrons (SSIES) experiment is a set of three sensors which include an ion drift meter, a retarding potential analyzer, and a Langmuir probe. Reduction of the SSIES data provides the ion density, temperature, and drift, and the electron temperature along the line of track. Measurements are provided on 4 second centers.

The DMSP SSJ/4 experiment is a set of 4 sensors which measure the precipitating electrons and ions along the satellite track. The total energy range covered for both

species is 30 eV to 30 keV in 20 energy channels. We use these measurements mainly to establish the equatorward boundary of the auroral zone.

3. Inversion of the EUV Images

As the technique to invert EUV images to produce a global mapping of the He^+ density is new, we include a detailed description of it. An EUV image is a two dimensional representation of the three dimensional plasmaspheric He^+ density profile. Under the assumption that the He^+ density is constant along L, the images can be inverted to produce two-dimensional density maps of the He^+ ion population in the geomagnetic equatorial plane. The inversion steps are outlined below.

The reduction of background and noise in the measured image is paramount in the inversion. Background increases the error in the absolute density estimate and noise is a major source of instability in the inversion. Removing the background and noise is a two-step process. First the instrument background is removed by computing the average count rate in each column of the image for a fixed rotation angle above and below the area of interest and subtracting this average from each pixel in the column. The resultant image is then passed through a despeckling algorithm. This removes active and isolated pixel clusters. The cluster size is nominally set to two pixels. Figure 1 shows the results of a typical background and noise removal. The figure on the left is the original EUV image cropped to show just the plasmasphere region. The figure on the right is the background and noise subtracted image. The inversion begins with the cleaned image.

The inversion uses an iterative approach in which an initial guess is modified repeatedly until it converges to a stable solution. The initial step in the iteration is the formation of the zero solution and density matrices. Both matrices have identical order and represent

a griding of the geomagnetic equatorial plane in L-shell (L) Geomagnetic Longitude (Λ) space. Both are over dimensioned to give them a higher spatial resolution than the EUV measurements. This is necessary both for stability and smoothness in the final solution.

The density profile matrix holds the current density He^+ profile. The profile is initialized to a simple power law in L with no Λ dependence as:

$$D = 10^{-.715L}$$

The zero solution matrix holds a status flag for each grid in the density matrix. This flag is either zero or one depending on whether the density of the grid is known to be zero or not. The matrix is initialized to all ones. Each EUV line of sight known to have a zero intensity is then mapped onto the zero solution matrix and those grids it passes through are set to zero. Since the instrument measures column density any pixel contained in a line of sight which has a zero total intensity associated with it must itself have zero density.

Also set up in the initialization are the variable grids in the density matrix. These are the grids that are modified in each step in the iteration process and from which the new density matrix is built in each iteration step. There is one variable grid representing each instrument line of sight. This keeps the problem from being over-constrained in the iteration phase of the inversion. The variable grids form a unique set of unknowns and are set to the grids containing the closest approach to the Earth of each line of sight.

Each iteration step begins with the construction of a synthetic image from the current density profile matrix. This is done in three steps. First the zero solution matrix is used to mask off the zero intensity grids in the density matrix. Second, the column density along each of the instrument lines of sight is then computed from the modified density matrix.

Any line of sight that is found to have only a single non-zero density value along it is set to zero and the zero solution matrix is updated. Lines of sight which have only a single non-zero value are generally noise which was not caught in the initial noise and background removal. Lastly, the column densities are modified by the instrument characteristics and the synthetic image is produced.

The mean square deviation between the synthetic and measured image is then computed and compared to mean square deviations computed in previous iteration steps to see if a convergence has been reached. If so, the iterations are terminated and the current density profile is returned.

When convergence has not be obtained the measured image is divided by the synthetic image to produce a correction value for each line of sight. The density matrix is rebuilt using only the variable grid values multiplied by their corresponding correction value. All unassigned grids in the density profile matrix are filled using a 2-D linear least square fit algorithm. Last the zero solution mask is applied to give the new density profile and a hot spot check is made. This is a search through the matrix for pixels which have intensities larger than their neighbors by some preset value. Such pixels are assumed to be or are in the process of becoming unstable. Their density is adjusted to the average value of their nearest neighbors. This concludes the iteration step which restarts with the computation of a new synthetic image.

It should be noted that the inversion makes no special treatment for either the day-glow contamination in the near Earth sunlit portion of the EUV images or the dimmer plasmasphere seen within the Earth's shadow. Both are treated in the inversion as real phenomena. This results in an anomalous density enhancement in the sunlit sectors and

a density depression directly anti-sunward of the Earth. The features are visible in all inversions.

4. ANALYSIS

Figure 2 shows the Dst and Kp indices over the two days of the storm. The storm begins with the sudden commencement which occurs between 03:00 and 04:00 UT on day 169. The main phase lasts for 6 to 8 hours with a minimum depression in Dst of about -58 nT occurring between 08:00 and 10:00 UT. Kp averages about 5 during this time. From hour 12 until the end of day 170 there is a slow recovery with Kp gradually falling to its pre-event level. At 15:00 UT on day 170 Kp jumps to 3+ and remains there until the end of the plot.

Figure 3 contains a selected set of 10 mappings of the global He^+ density covering the time period in Figure 1. Time runs left to right and top to bottom. Each plot is a 6x6 R_E Earth centered cut through the geomagnetic equatorial plane. The white centered region is the Earth which is not included in the inversion. The narrow bright region seen on the sunlit side of the Earth is airglow contamination while the depression in the density seen just anti-sunward of the earth is due to the Earth's shadow.

The first plot in the figure shows the plasmasphere prior to the onset of the storm (between 02:56 and 03:06 UT). The storm onset time was established from a significant jump in the EUV background in the image taken during this time period (and continuing into the next image) that is the result of the arrival of the high energy solar protons at the storm onset. The plot depicts the local quiet-time plasmasphere for this event with the plasmasphere extending out to about 5 R_E. The next image, taken two hours after the storm onset, shows the beginning of erosion of the plasmasphere. By the third image,

at which time the storm has entered the main phase, the plasmasphere has reached its minimum extent of about 3.5 R_E. For the next 20 or so hours the plasmasphere stays in this minimal or disturbed state and then gradually begins to expand not quite reaching its pre-event size by the end of day 171.

Figure 4 shows selected mappings of the ion differential energy flux in the magnetic equatorial plane between 06:23 UT on day 169 to 04:26 UT on day 170 (basically from the start of the main phase and into the recovery). The mappings are inversions of 8.6 keV centered images from the MENA NAI experiment. Inversions were produced using data averaged over 5 satellite spins to match the base EUV time resolution of 10 minutes. The individual plots use the same spatial layout as the He^+ density plots in Figure 2 ($\pm 6.0\, R_E$) even though the inversions are carried out to 8.0 R_E. Similar plots exist for each of the 6 HENA energy channels covering the energy range $10 - 81$ keV. The ions follow the standard picture of the ring current within a storm: an ion injection from the tail, followed by earthward convection coupled with a gradient curvature drift to build the ring current, then fragmentation as the ion source turns off and the eventual decay.

Each DMSP spacecraft makes 2 cuts through the plasmaspheric latitudes every 101 minutes. These are either noon-midnight or dawn-dusk cuts depending on the satellite. Figure 5 shows a southern hemisphere pass of the F12 DMSP satellite. It illustrates the more important storm time features observed in the auroral and sub-auroral ionosphere.

The ambient electron temperature fluctuates within both crossings of the auroral zone which are located by the precipitating ion and electrons. At higher time resolution the changes in temperature are reasonably correlated with changes in the intensity of the electron precipitation. The correlation is used to distinguish auroral from sub-auroral

heating. At 13:25 UT there is a region of enhanced temperature in the sub-auroral region in the dusk sector. There is no comparable enhancement in the dawn sector. The lack of ion precipitation accompanying the sub-auroral temperature enhancement is not limited to this pass. No ion precipitation is seen in conjunction with any sub-auroral temperature enhancements within the two day storm period. This is important because proton precipitation is expected to accompany heating produced in the damping of ion cyclotron waves *Cornwall et al.* [1971]. There is also a small density trough associated with the temperature enhancement in the figure, but this is not the case in the majority of passes. Density troughs in conjunction with the enhanced electron temperatures are generally required for SAR arc formation.

The location of the sub-auroral heating with respect to the plasmapause varies considerably over the time period studied. Examples are seen in Figures 6 and 7. Both figures show complete trans-equatorial DMSP crossings with sub-auroral heating in both hemispheres. Figure 6 is a dawn sector crossing and Figure 7 a dusk sector crossing. The two sub-auroral heating events in each figure are separated by at most 30 minutes in time. Six sets of these plots can be assembled from the three DMSP spacecraft each orbit (101 min).

The trace of the electron flux (cyan) delineates the auroral and sub-auroral regions in each plot. The rapid rise in the electron flux is a good indicator that the satellite has crossed from the sub-auroral into the auroral zone. Enhancements in the electron temperature (blue) prior to this rise are sub-auroral heating events while features after the rise are the result of auroral electron precipitation. The plasmapause is indicated by the steep fall in the He^+ density trace (red).

Both heating events in Figure 6 occur significantly Earthward of the plasmapause. This is a common characteristic in the dawn sector and also at times when the plasmapause and the equatorward auroral boundary coincide or nearly coincide in L (for example see Figure 8).

Dusk sector events are more likely to have their outer edge in the vicinity of the plasmapause with the position of the inner edge sometimes occuring deep in the plasmasphere. Figure 7 shows a complex example of ionospheric heating from a dusk sector crossing. The satellite crosses a bulge in the plasmasphere which extends to nearly 5 R_E in the pre-midnight sector. There appear to be multiple individual heating events in both the southern and northern hemisphere plasmasphere crossings. The first heating event occurs near L = 4.3 just after crossing into the bulge. This is followed almost immediately by a larger heating event centered at an L = 3.5. Both of these events occur within the bulge region. There is also a third event which can be seen at L 2.3 in the southern hemisphere (top set of plots) and may be hinted at in the northern hemisphere portion of the pass. This event is well inside of the plasmapause, on the order of the heating events seen in Figure 6.

Figures 8 through 12 show the relationship of selected sub-auroral temperature enhancements with the equatorial ion flux. Figure 8 shows a midnight sector pass during the main phase of the storm. The heating is narrow in extent and separated from the plasmapause by more than 0.5 R_E. The latter separation is common when the equatorial edge of the auroral zone nearly coincides with the plasmapause as it does in this case. The ring current overlaps the temperature enhancement at all energies.

Figure 9 shows an F13 dusk sector pass that closely follows the F15 midnight sector pass in Figure 8. Here there is a broad sub-auroral temperature enhancement which almost reaches the plasmapause. The location of the inner edge of the heating is almost identical to that in Figure 8.

Figures 10 and 11 show a pair of nearly coincident dawn and pre-midnight sector passes during the storm's recovery phase. By this time the ion injection has stopped and the ring current shows a distinctive minimum centered on the midnight sector. The two passes show major differences in the locations and conditions under which the ionospheric heating takes place. There is an almost $1R_E$ separation in L between the two events. The dawn sector event, as expected, occurs well off the plasmapause while the dusk sector event is just interior of it. Even more striking is the relationship of each event to the ring current. The dusk event shows about the same relationship as seen in the previous two figures, however the dawn sector event shows the ring current overlap occurring at only the lowest energy channel which may indicate that the higher energy ions play little or no role in the heat flux formation. The reason the ring current does not fully overlap the region of heating in Figure 10 is due to a cut off at 2.0 R_E in the ion inversion code. Undoubtedly the ions do extend to lower L in this case.

Figure 12 shows another dawn sector crossing. As in Figure 10 the heating is offset from the plasmasphere and extends to even smaller L. The only overlap is with the low energy ring current. Again the 2 R_E cut off in the inversion is responsible for the ring current ions not fully overlapping the heating region.

The final plot in the series is again a dusk sector pass occurring very near the end of the recovery period. With the exception of in the pre-noon sector, the intensity of the ring

current ions has begun to decay. The decay is limited mostly to the central ring current as comparisons of this figure to previous figures will show that the intensity of the inner edge of the ring current where it overlaps the sub-auroral heating regions has changed little. The heating occurs over nearly 1.5 R_E in L, extending from near an L of 2.5 to the plasmapause at L of 4 and appears to be centered on a small increase in the local plasmaspheric density.

5. DISCUSSION

The variability in the magnetospheric plasma parameters under which the heating of the ambient topside electrons is observed to take place makes it difficult to point to a primary mechanism. Coulomb collisions occur where ever the ring current overlaps the plasmasphere. The amount of energy exchanged between the two populations is proportional both to the number of scattering centers and to the energy and mass of the constituent ring current ions *Kozyra et al.* [1997]. If the mechanism responsible for the heat flux were Coulomb collisions alone one would then expect some heating to occur over the entire overlap region. But often the heating is extremely localized within the overlap region. This suggests that while the Coulomb collision may be partly or wholly responsible for the heating of the plasmaspheric electrons, another mechanism transfers the heat into the ionosphere, a mechanism which acts only under a restricted set of conditions.

One candidate that suits such a criteria would be a plasma instability. The growth rates of most instabilities including the electromagnetic ion cyclotron (EMIC) instability are sensitive to the local hot to cold plasma density ratio [*Gamberoff and Neira*, 1983]. The dependence on the density ratio would lead to a naturally bounded region within the area defined by the overlap of the ring current and plasmasphere. Figures 14 through 18

show the ratio of hot ring current to cold plasmasphere He^+ density (R_{HC}) as a function of the sub-auroral ionospheric temperature along the satellite track for the heating events in Figures 8 through 13. Data from the different L-shell intervals are plotted as different symbols which are annotated in the upper right of the figure. The gray background defines the upper limits of the plotted points and is included simply to make the features in the figures easier to discern.

The ring current density was computed by first converting the ion number flux to units of distribution function (sec^3/cm^6) and then integrating over the distribution function under the assumption of isotropy. The integrals were carried out over the energy range 5 keV to 50 keV. The ion inversions above this energy range were not always stable over the time range being studied and so were not included in the integral. Also, the small overlap in in energy between the MENA and HENA energy channels was not corrected for. This slightly overestimates the hot ion density. The error is negligible given the assumption of isotropy and the limited energy range of the integrals.

As a whole the plots show that ionospheric heating takes place over relatively narrow range of R_{HC}. Further, the ranges are easily grouped according to the sector in which the heating is observed. In all dusk and pre-midnight sector events (Figures 14, 15, 17, and 19), the heating occurs when R_{HC} is centered near 0.001 (0.1%). In dawn sector events (Figures 16 and 18) the peak is at a much lower value, closer to $(1-5)\times 10^{-5}$. The lack of a physical peak in the dawn sector ratios is the result of the 2.0 R_E cut off in the inversion of the MENA neutral images so that data at L less than 2 is not included in the plot.

The difference in the ratios between the dusk and dawn sector events could have several origins, including a difference in the physical processes under which the heat flux is formed.

In dawn sector passes only the lowest ring current energy band overlaps the region where the heating is observed. This results in a lower density and therefore in a lower ratio. But even computing the dusk side ratios using only the lowest energy band still leaves them a factor of 10 above those computed in the dawn side passes. A second reason for the difference could be that we are looking only at a ratio formed from the total hot ion density and the cold He^+ ion density. Different values will be obtained using different cold and hot ion species. This is not expected to result in any great divergence within either the dawn or dusk grouped ratios alone but it might reduce the difference between the two groups. Differences in the dusk-dawn ring current composition can be large [*Fok et al.*, 1993].

While not conclusive, the similarity in the values of the ratios in either the dawn or dusk grouped data points toward an instability as the primary mechanism in producing the downward heat flux. The criterion of a proper density ratio, however, is only one of probably several that must be satisfied before the instability would become active. It cannot be overlooked that many passes, particularly in the dawn and pre-noon sectors show a significant ring current overlap of the plasmapause and no observed ionospheric heating in the electrons. These passes contain a full spectrum of R_{HC} yet the transfer mechanism is not active.

6. Conclusions

We have presented examples showing the relationship of the topside heating of the sub-auroral ambient electrons with the plasmasphere and ring-current for the June 18/19 2001 magnetic storm. There are several interesting features observed in these events:

1. Sub-auroral heating events do not necessarily occur in the vicinity of the plasmapause but can be embedded within the plasmasphere. Such events are generally observed in the dawn sectors and when the equatorward edge of the auroral oval nearly coincides with the plasmapause.

2. The heating occurs on field lines populated by both ring current and plasmasphere plasma. In the dawn sectors these field lines include only the lowest observed ring current energies. In the dusk sectors the ring current ions will extend in energy to beyond 50 keV.

3. The overlap of the plasmasphere and ring current often exceeds the extent of the observed ionospheric heating. This would seem to imply that while Coulomb collisions may act as a heat source it is probably not the transfer agent.

4. The regions over which temperature enhancements are observed can be characterized by a nearly constant R_{HC}. This is consistent with an instability as the heat transfer mechanism.

5. Heating in the dawn ans dusk sectors are characterized by different R_{HC}values which may indicated that different mechanisms are responsible for the observed heat fluxes.

6. The lack of ion precipitation within thermal enhancements raises the question about the involvement of EMIC waves in the generation of the heat flux.

The overall picture of the heat generation and transfer is not complete. There are still several outstanding questions. If the transfer of heat is driven by EMIC waves where is the accompanying ion precipitation? If EMIC waves that are not acting as the driver of the heat flux, what is? Finally, what consititutes the parameter set that will allow accurate predictions of sub-auroral heating?

Acknowledgments.

The authors acknowledge support from subcontracts under NASA contract NAS5-96020 to Southwest Reseach Institute. The authors would also like to acknowledge the Center for Space Sciences at the University of Texas at Dallas for the DMSP thermal plasma data and the National Geophysical Data Center for the long-term archive by the Air Force Weather Agency for all the DMSP data used in this paper.

References

Chandra, S. E., J. Maier, and P. Stubbe, The upper atmosphere as regulator of subauroral red arcs, *Planet. Space Sci.*, *20*, 461, 1972.

Cole, K. D., Stable auroral red arcs, sinks for energy of Dst main phase, *J. Geophys. Res.*, *70*, 1689, 1965.

Cole, K. D., Coulomb collisions of ring current particles -indirect source of heat for the ionosphere, *Tech. Rep. X-621-75-108*, Goddard Space Flight Center, Greenbelt, MD, 1975.

Cornwall, J. M., F. V. Coroniti, and R. M. Thorne, Unified theory of SAR arc formation at the plasmapause, *J. Geophys. Res.*, *70*, 4428, 1971.

Erlandson, R. E., T. L. Aggson, W. R. Hogey, and J. A. Slavin, Simultaneous observations of subauroral electron temperature enhancements and electromagnetic ion cyclotron waves, *Geophys. Res. Lett.*, *29*, 1723, 1993.

Fok, M. C., J. U. Kozrya, A. F. Nagy, and T. E. Cravens, Lifetime of ring current particles due to coulomb collisions in the plasmasphere, *J. Geophys. Res.*, *96*, 7861, 1991.

Fok, M. C., J. U. Kozrya, A. F. Nagy, C. E. Rasmussen, and G. V. Khazanov, Decay of equatorial ring current ions and associated aeronomical consequences, *J. Geophys. Res.*,

98, 19,381, 1993.

Foster, J., M. J. Bounsato, M. Medillo, D. Nottingham, F. J. Rich, and W. Deng, Coordinated stable auroral red arc observations: Relationship to plasma convection, *J. Geophys. Res.*, *99*, 11,429, 1994.

Gamberoff, L., and R. Neira, Convective growth rate of ion cyclotron waves in a $H^+ - He^+$ and $H^+ - He^+ - O^+$ plasma, *J. Geophys. Res.*, *88*, 2170, 1983.

Hasagawa, A., and K. Mima, Anomalous transport produced by kinetic Alfvén wave turbulence, *J. Geophys. Res.*, *83*, 1117, 1978.

Jordanova, V. K., R. M. Thorne, C. J. Farraugie, , Y. Dotan, J. F. Fennell, M. F. Thompsen, G. D. Reeves, and D. J. McComas, Ring current dynamics during the $13-18$ July 2000 storm period, *Solar Phys.*, *204*, 361, 2001.

Khazanov, G. V., K. V. Gamayunov, and V. K. Jordanova, Self-consistent model of magnetopsheric ring current and electromagnetic waves: The 2-7 may 1998 storm, *J. Geophys. Res.*, *108*, 1419, 2003.

Kozyra, J. U., T. E. Cravens, A. F. Nagy, M. O. Chandler, L. H. Brace, B. A. Emery, and S. D. Shawhan, Characteristics of a stable auroral red arc event, *Geophys. Res. Lett.*, *9*, 973, 1982.

Kozyra, J. U., E. G. Shelley, R. H. Comfort, L. H. Brace, T. E. Cravens, and A. F. Nagy, The role of ring current O^+ in the formation of stable auroral red arcs, *J. Geophys. Res.*, *92*, 7487, 1987.

Kozyra, J. U., A. F. Nagy, and D. W. Slater, High-altitudes energy source(s) for stable auroral red arcs, *Rev. Geophys.*, *35*, 155, 1997.

Lanzerotti, L. J., A. Hasagawa, and C. G. Maclennan, Hydromagnetic waves as a cause of a SAR arc event, *Planet. Space Sci.*, *26*, 777, 1978.

Lundblad, J. Å., and F. Søraas, Proton observations supporting the ion cyclotron wave heating theory of SAR arc formation, *Planet. Space Sci.*, *26*, 245, 1978.

Mitchell, D. G., et al., High energy neutral atom (HENA) imager for the IMAGE mission, *Space Sci. Rev.*, *91*, 67, 2000.

Norton, R. B., and J. A. Findley, Electron temperature and density in the vicinity of the 29 September 1967 middle latitude red arc, *Planet. Space Sci.*, *17*, 1867, 1969.

Perez, J. D., M. C. Fok, and T. E. Moore, Deconvolution of energetic neutral atom images of the Earth's magnetosphere, *Space Sci. Rev.*, *91*, 421, 2000.

Pollock, C. J., et al., Medium energy neutral atom (MENA) imager for the IMAGE mission, *Space Sci. Rev.*, *91*, 113, 2000.

Roelof, E. C., and A. J. Skinner, Extraction of ion distributions from magnetospheric ENA and EUV images, *Space Sci. Rev.*, *91*, 437, 2000.

Sandel, B. R., et al., The extreme ultraviolet imager investigation for the IMAGE mission, *Space Sci. Rev.*, *91*, 197, 2000.

Thorne, R. M., and R. B. Horne, Modulation of electromagnetic ion cyclotron instability due to interation with ring current, *Space Sci. Rev.*, *102*, 14,155, 1997.

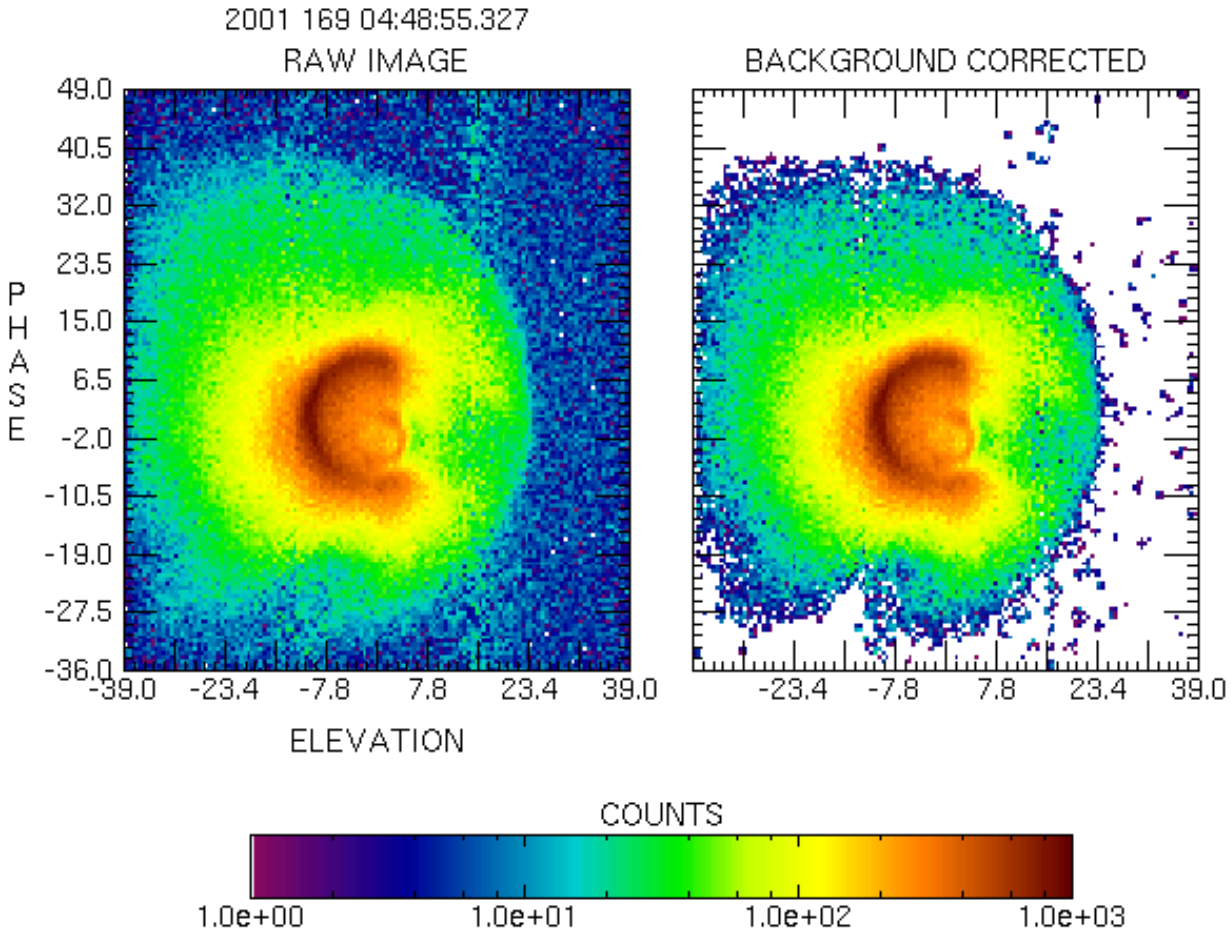

Figure 1. Measured EUV image (left) and background subtracted image (right)

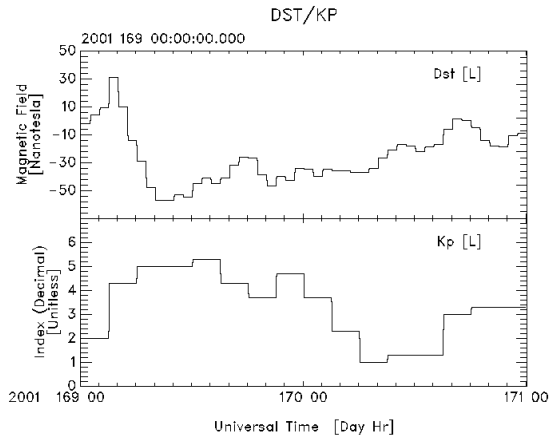

Figure 2. Dst and Kp indices across the time of the storm. Sudden commencement occurs close to 04 UT on day 169.

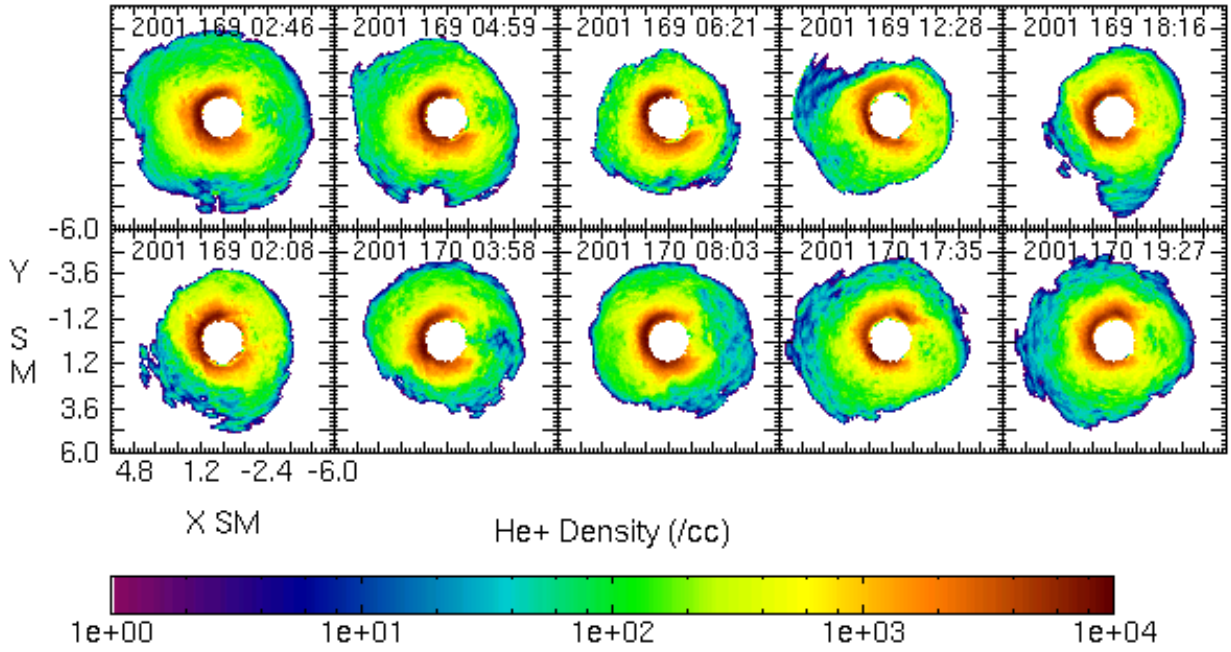

Figure 3. Inversions of selected EUV images across the storm time period. In each image the sun is to the left, dawn is up, dusk is down, midnight is to the left. Plots depict the He^{+}ion density in the geomagnetic equatorial plane.

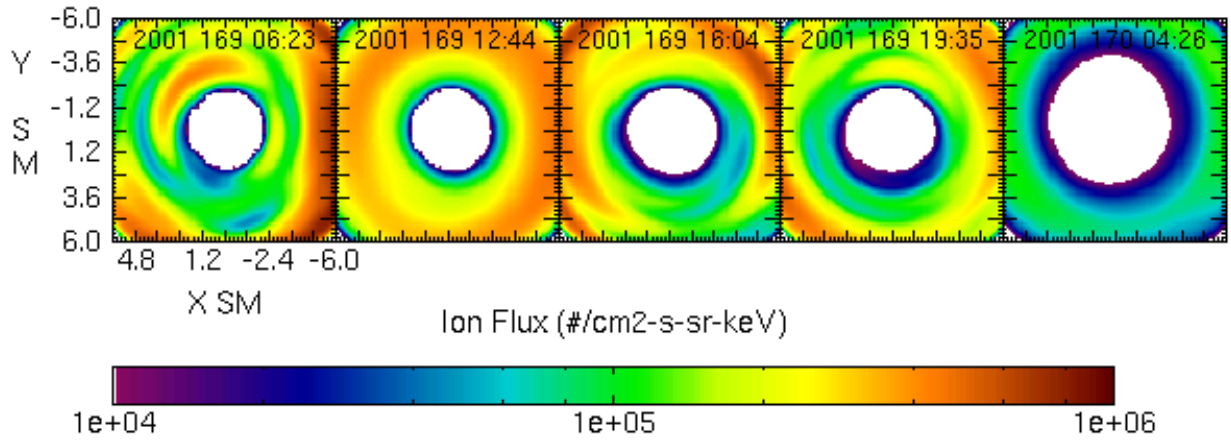

Figure 4. Selected inversions of the MENA 5.1 − 12.0keV neutral images across the storm time. Plots depict ion flux in the geomagnetic equatorial plane.

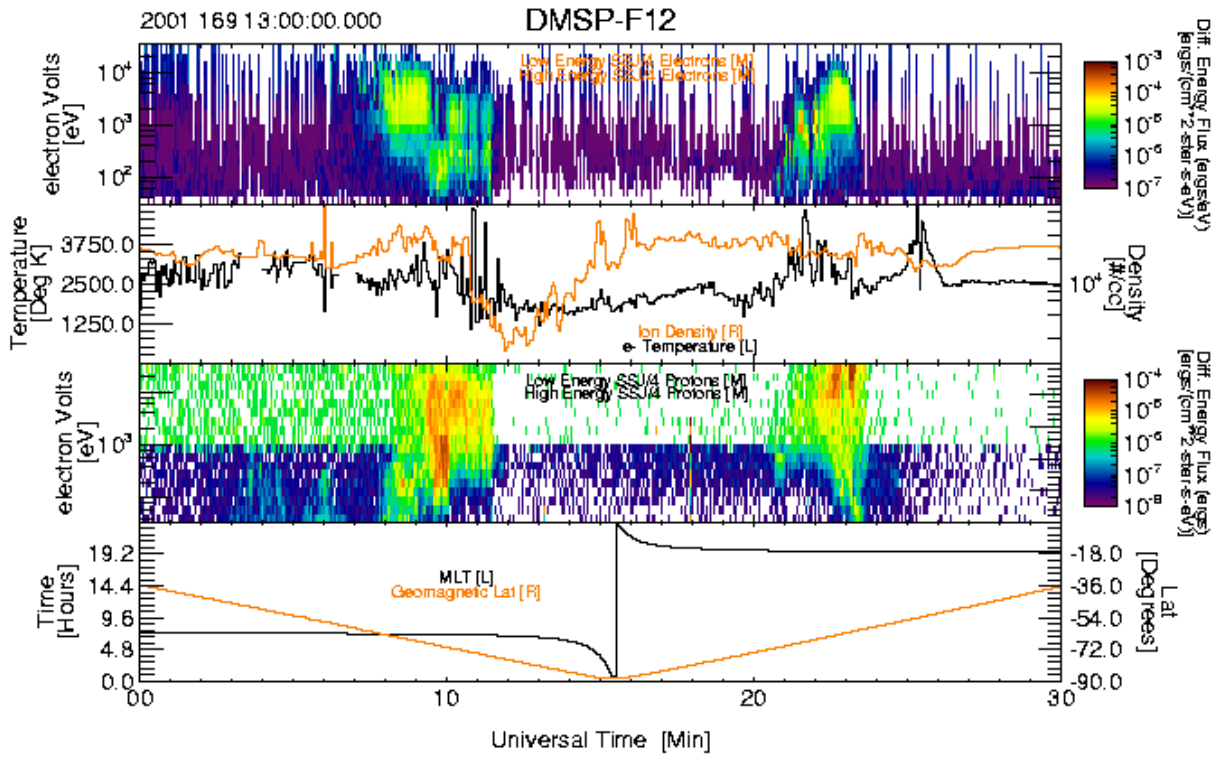

Figure 5. DMSP data showing a complete dawn to dusk southern hemisphere pass of F12. Top spectrogram shows precipitating electrons and middle spectrogram shows precipitating ions. Both data sets are plotted in units of differential energy flux. Upper set of line plots shows the ambient electron temperature (black) and the ion density (orange). Lower set of line plots shows the satellite magnetic local time (black) and geomagnetic latitude (orange). An enhancement in the sub-auroral electron temperature is centered on 13:25 UT

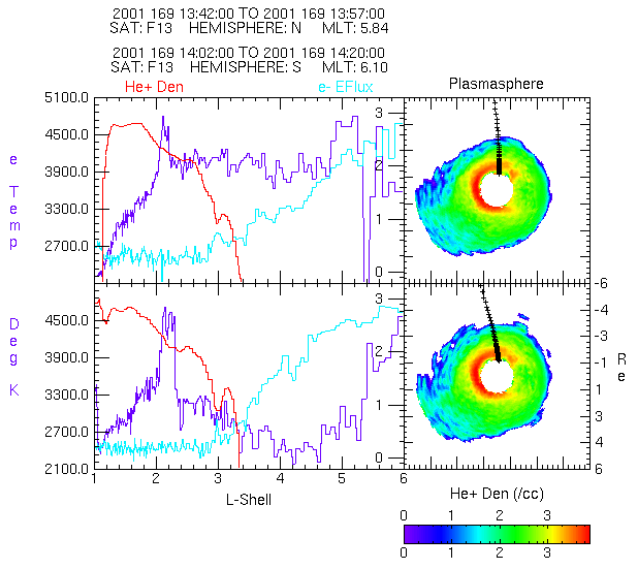

Figure 6. Consecutive north/south dusk sector crossings of the plasmasphere. Southern hemisphere portion of the crossing is covered in upper plots and the northern hemisphere portion of the crossing is covered in the lower plots. Traces in the left-hand plots are the plasmasphere He^+ density (purple), the ionospheric temperature (blue), and the precipitating electron flux between 1 and 14 keV (cyan) along the satellite track. The scale for the plasmasphereic density trace is given along the right-hand axis. The electron flux trace has units of $erg/cm^2 - s$ and is plotted against a logarithmic scale from 10^{-1} to 10^{-5} which is not explicitly shown in the plots. The right-hand plots show the equatorial projection of the plasmaspheric He^+ density at the time of the temperature enhancement overlaid by the satellite track. General information describing the plots is given in the two top labels (uppermost label goes with the top pair of plots). This information includes the beginning and ending time of the orbit track, the satellite from which the data was taken, the hemisphere in which the data was taken (North or South), and the Magnetic Local Time (MLT) at a point midway through the time period.

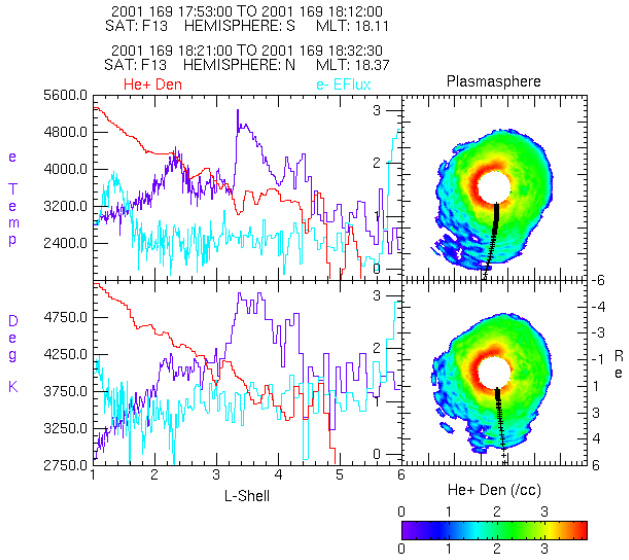

Figure 7. Identical to Figure 6 but for a dawn sector crossing with the northern hemisphere portion of the pass depicted in the upper set of plots and the southern hemisphere portion in the lower set.

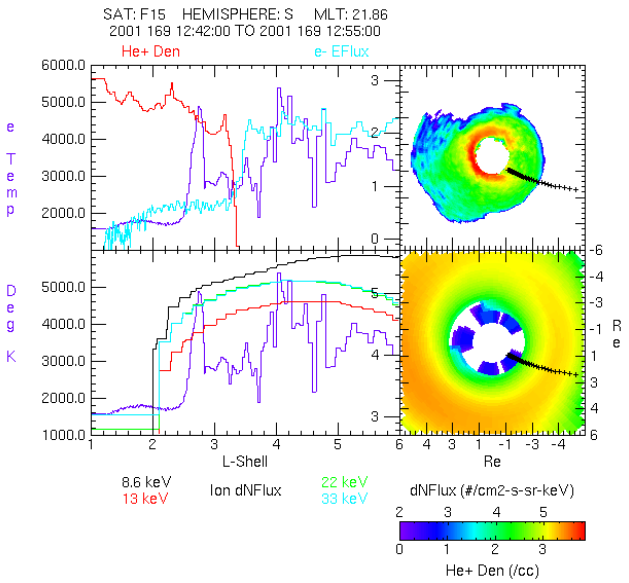

Figure 8. Relationship of the sub-auroral heating to the ring current ions. Upper two plots have identical format to those in Figures 6 and 7. Lower set of traces are the electron temperature (purple) together with the MENA 8.6 keV (black) and the HENA 13 (red), 22 (green) and 33 (cyan) keV ion fluxes along the satellite track. The fluxes are plotted in units of differential number flux ($/cm^2 - s - sr - keV$) and are scaled according to the right-hand axis in the plot. Lower right-hand plot is the equatorial ion flux map generated from the HENA 22 keV centered neutral image with the satellite track overlaid.

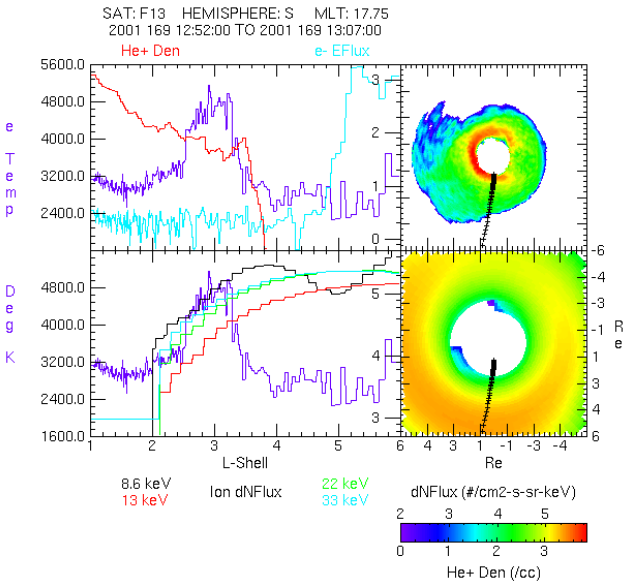

Figure 9. Identical in format to Figure 8 showing the sub-auroral heating in the dusk sector about 12 minutes after the event seen in Figure 8.

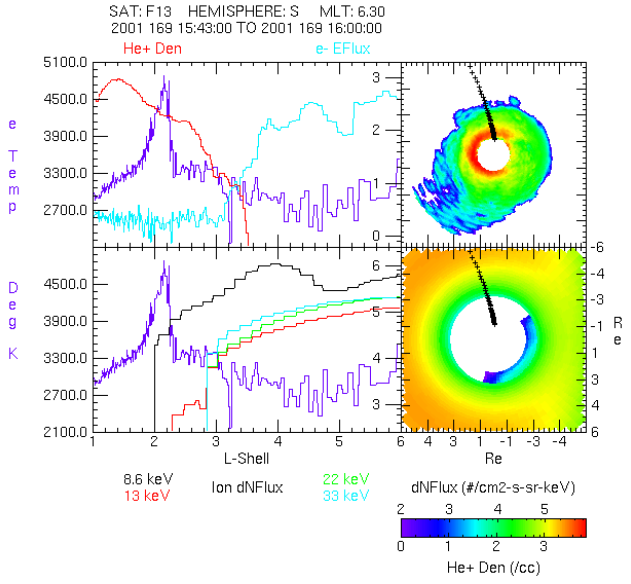

Figure 10. Dawn side example of a sub-auroral temperature enhancement occurring during the recovery period. There is only minimal overlap of the ring current with the region in which the heating occurs and then only at the lowest energies.

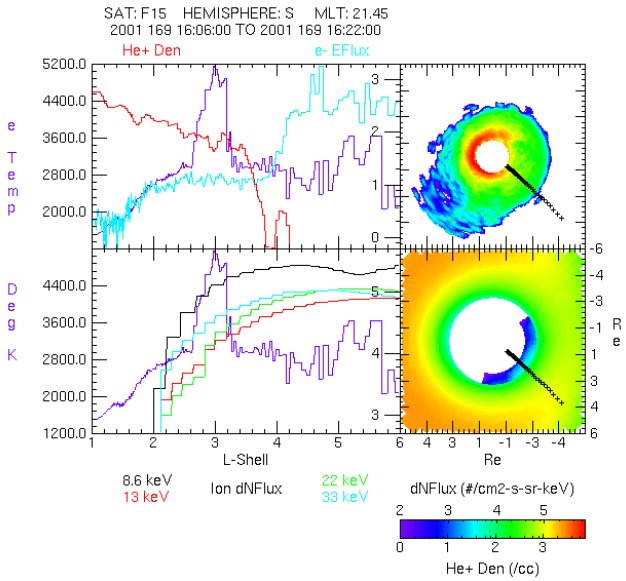

Figure 11. A nearly coincident observation of a sub-auroral temperature enhancement in the pre-midnight sector to the observation in Figure 10 showing the difference in the ring current overlap.

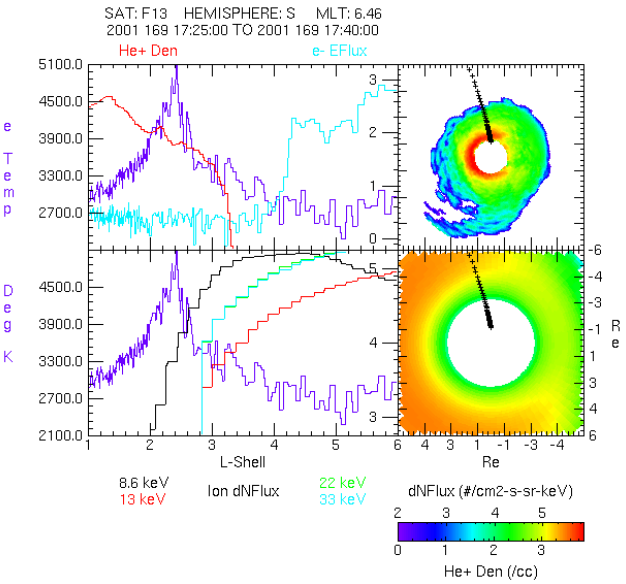

Figure 12. A dawn sector crossing showing again the offset of the heating from the plasmapause. The heating extends to even lower L than in Figure 10.

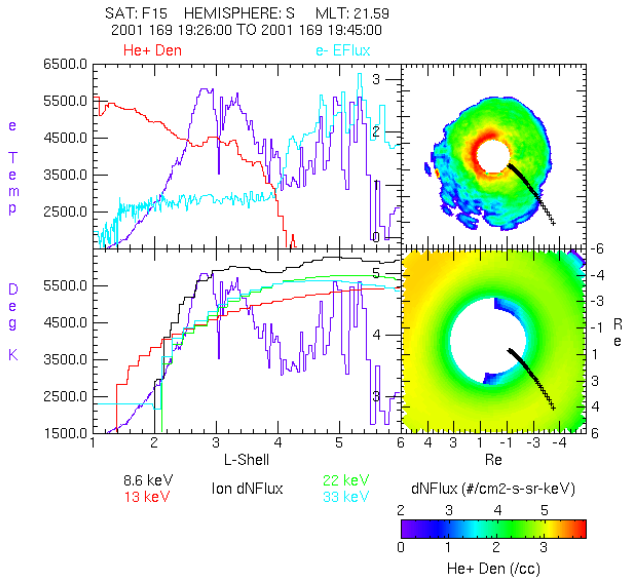

Figure 13. Heating even near the end of the storm recovery. The heating occurs over a very large extent in L, extending from near the plasmapause to well into the plasmasphere.

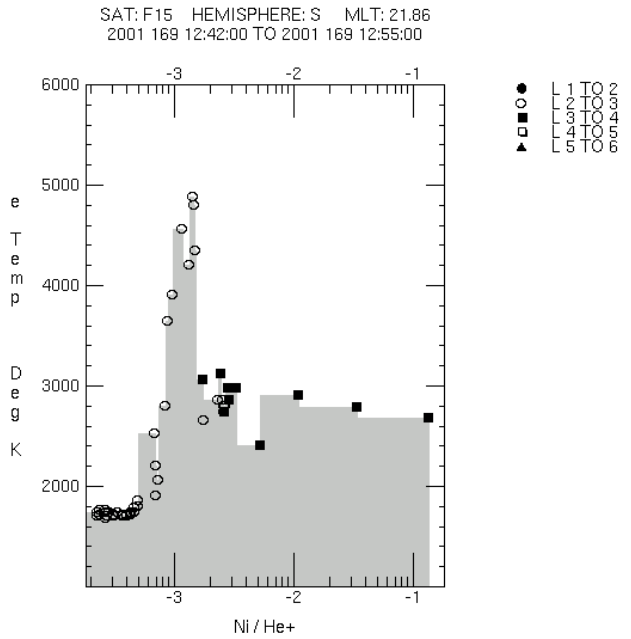

Figure 14. Topside electron temperature as a function of the hot to cold ion density ratio along the satellite track in Figure 8. Symbols indicate the L shell from which the ratios were obtained.

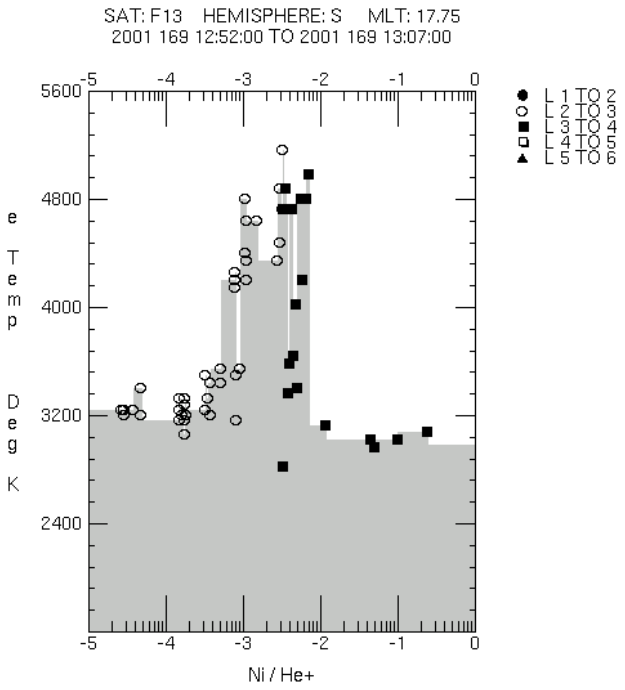

Figure 15. Identical to Figure 14 but covers the satellite track from Figure 9.

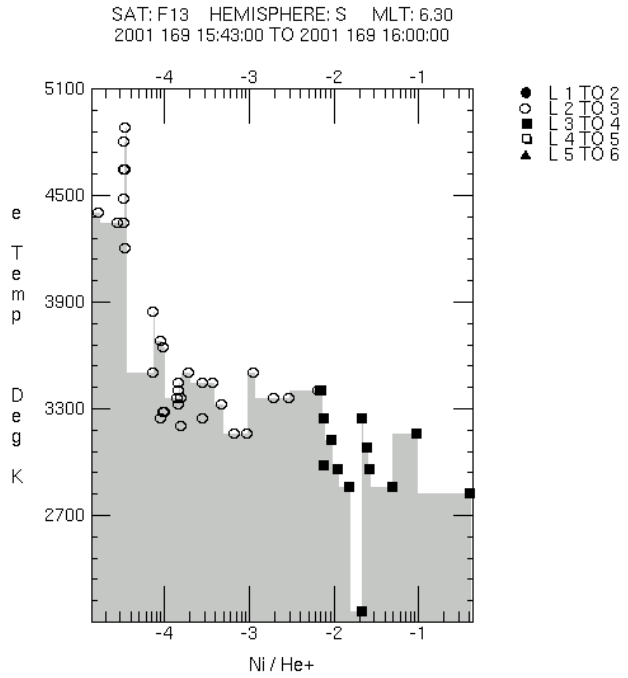

Figure 16. Identical to Figure 14 but covers the satellite track from Figure 10.

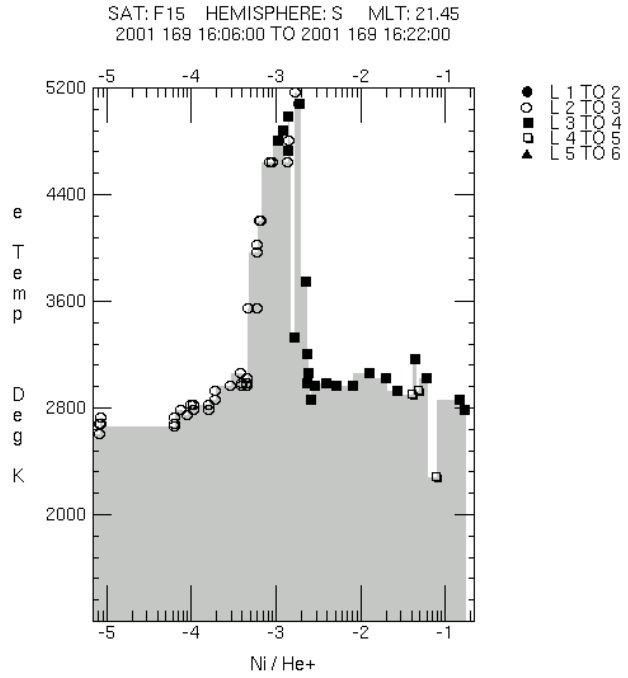

Figure 17. Identical to Figure 14 but covers the satellite track from Figure 11.

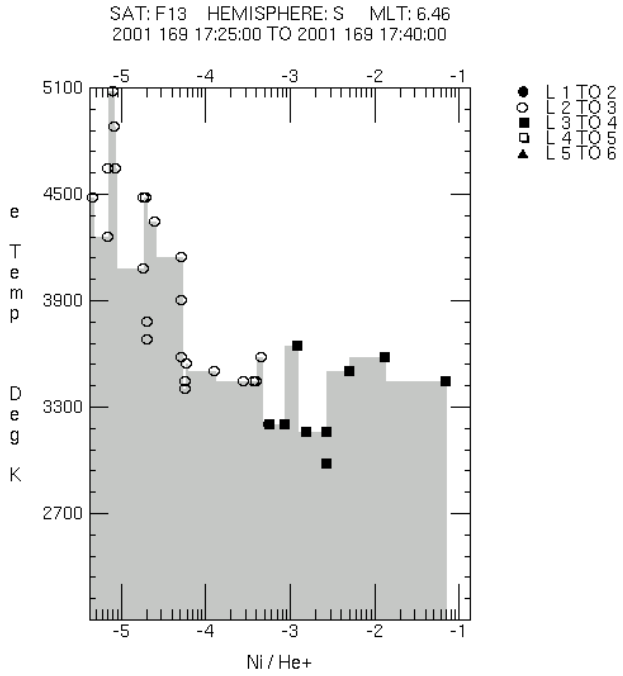

Figure 18. Identical to Figure 14 but covers the satellite track from Figure 12.

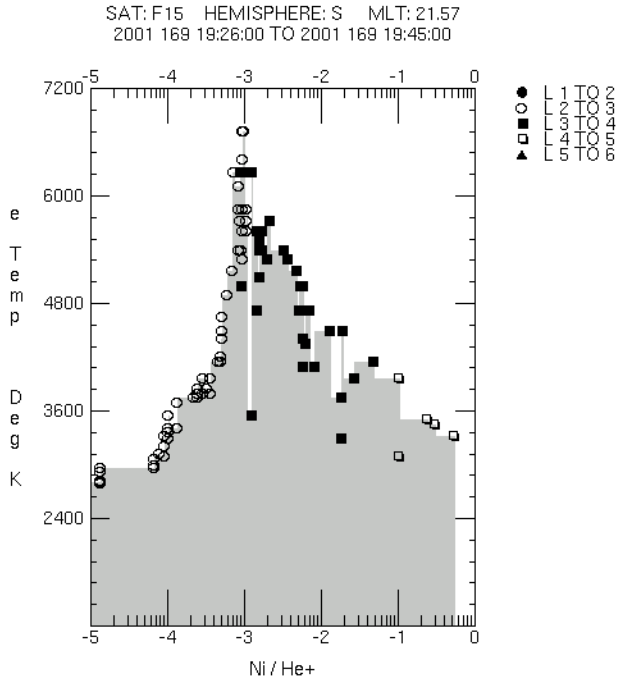

Figure 19. Identical to Figure 14 but covers the satellite track from Figure 13.